

Optimization of a Dense Plasma Focus Device as a Light Source for EUV Lithography

Igor V. Fomenkov, William N. Partlo, Richard M. Ness, I. Roger Oliver, Stephan T. Melnychuk, Oleh V. Khodykin, Norbert R. Böwering (Cymer, Inc. 16750 Via Del Campo Ct, San Diego, CA 92127).

ABSTRACT

Since the initial demonstration of EUV emission with Xenon as a source gas in Cymer's Dense Plasma Focus (DPF) device, significant effort has been spent exploring the parameter space for optimization of efficient generation of EUV radiation. Parameters included in this investigation are He and Xe pressure and flow rates, electrode geometries, pre-ionization characteristics, and duty factor related performance issues. In these investigations it was found that the location of the He (buffer gas) and Xe (working gas) gas injection ports as well as the pressures and flow rates of the gas mixture components had a strong impact on EUV emission efficiency. Additional constraints on the gas recipe are also derived from gas absorption of the EUV radiation and the desire to provide debris mitigation properties. Best results to date have been obtained with an axially symmetric buffer gas injection scheme coupled with axial Xe injection through the central electrode. The highest conversion efficiency obtained was 0.42% at 12.4 J of input energy. Measurements of energy stability show a 10% standard deviation at near optimum EUV output. The matching of the drive circuit to the pinch as determined by the damping of the voltage overshoot waveforms was found to depend strongly on the He and Xe pressures.

Energy Dispersive X-Ray (EDX) analysis of the debris emitted from the source shows that the primary sources of the debris are the central electrode and the insulator. No evidence of cathode material has been found. In addition to efforts toward more efficient operation, first phase efforts of thermal engineering have been undertaken, which have led to continuous operation at 200 Hertz with conventional direct water cooling. The system can be operated at higher repetition rates with proportionally lower duty cycles. The data will show the distribution of thermal power throughout the whole system. This more detailed understanding of the thermal power flow allows us to better determine the ultimate high volume manufacturing potential of this source technology.

Keywords: EUV Lithography, EUV light source, Dense Plasma Focus, Xe emission.

1. INTRODUCTION

With the emergence of EUVL as the chosen technology for next generation lithography systems, significant effort has been spent in developing light sources to meet the challenging requirements of the stepper manufacturers [1] as well as meeting the aggressive road maps of the end users for high volume manufacturing [2].

Recently discharge-produced plasmas [3-5] have demonstrated significant gains in performance with conversion efficiencies approaching those of the more mature laser produced plasma sources [6]. The particular specifications which the light sources must meet are tightly coupled with the design of the entire illumination system. Key source parameters which must be measured are: operating wavelength, in-band EUV power, out-of-band power, source size; maximum collectible angle, high repetition rate scaling; pulse to pulse repeatability and debris generation from plasma facing components.

Our early efforts in DPF development [7] were directed at developing the basic pulsed power technology required to drive a source of this type. High conversion efficiency was demonstrated with Li vapor as the active radiating element at high stored energy (25J). These stored energies were too high for practical scaling to high repetition rate operation. Development of the 4th generation machine allowed us to use Xe as the active species [8]. Our recent efforts have been focussed on optimizing the performance of the DPF with Xe as the source gas. To facilitate this effort we have set up six new source development labs to address key aspects of the source. Currently, we have facilities dedicated to investigation of pulsed power development, plasma initiation and characterization, EUV metrology, debris mitigation and characterization, thermal engineering, and collector optics development.

In this paper we will present some of our recent advances in these areas. We will discuss efforts at improving the conversion efficiency of the source, and its dependence on gas recipe. We will present measurements of the source size measured at peak conversion efficiency, and present data on high repetition rate operation and energy stability. We will discuss the characterization by EDX analysis of the debris ejected from the plasma electrodes, and present a simple technique, based on optical absorbance measurements of thin films, as a tool for comparing debris deposition rates for various mitigation arrangements. Finally we will present a concept for thermal management of the source and discuss the partition of input energy between the electrodes.

2. DENSE PLASMA FOCUS SYSTEM DESCRIPTION

As described previously [8], the current generation of Dense Plasma Focus system developed by Cymer utilizes a power system with solid-state switching and several stages of magnetic pulse compression, similar to that used in Cymer's excimer lasers, in order to generate the high voltage, high peak power pulse required by the DPF to generate EUV light. These systems begin with a charging voltage of 1300 V and generate an output pulse applied to the DPF of ~ 4 kV with a risetime of less than 50 ns. Although current measurements have not yet been directly performed, circuit simulations based on the voltage waveforms from typical experiment operation predict that the output DPF drive current peaks at a value of ~ 50 kA, with a dI/dt of 675 kA/ μ s. It is this combination of high peak current and high dI/dt that allow the DPF to function efficiently.

Six DPF machines currently exist at Cymer, being used for a variety of experiments on system optimization, pre-ionization, power system development, debris mitigation, thermal management, and collector design. For those experiments not requiring high repetition rates (~ 1 kHz and above), charging power for these machines is simply provided by resistive charging from a set of DC power supplies. Those DPF systems that do require high rep-rate capability are being charged with a resonant charging system which charges the initial energy storage capacitor, C0, to a voltage of 1300 V in less than 250 μ s. These resonant charging systems also provide energy recovery, storing the energy which is not utilized by the DPF or dissipated in heat and using this recovered energy for the next pulse. This reduces the amount of power required by the main power supply and also helps with other issues such as thermal management.

3. IN-BAND AND OUT-OF BAND EUV MEASUREMENTS AT LOW REPETITION RATES

In this section we present an overview of measurements performed on one of Cymer's low-duty-factor sources operated at less than 50 Hz. We will discuss the dependence of the EUV output and conversion efficiency on gas recipe, present data on the out of band emission, and show measurements of the source size and position stability.

Over the past year significant progress has been made in understanding some of the empirical dependencies of the EUV output on electrode geometry and gas dynamics issues. Significant changes in the apparatus, as compared with earlier generations include a new cathode design which allows gas to be injected symmetrically around the anode region, and a system for injecting He and Xe mixtures through the anode electrode.

The gas delivery system was modified to allow combinations of He and Xe to be injected into different sections of the DPF system. A schematic of this system is shown in Figure 1. Gas control is performed via two mass flow controllers and a high-accuracy capacitance manometer. The system is operated in a constant-pressure mode. Xe is injected in a constant-flow mode, and He makeup gas is added in order to reach the target operating pressure. In this mode the He flow rate depends on the pumping speed of the system. Dependence on gas flow rates was investigated by testing different pumping configurations.

All measurements of in-band EUV energy were performed with diagnostic vessels similar to the FOM "flying circus" configuration [9]. Radiation emitted from the pinch along the axis passes through an aperture into a differentially pumped diagnostic chamber. Gas absorption in the measurement vessel is minimized by maintaining the pressure below 5 mTorr. For these measurements the diagnostic vessel entrance was located 5 cm from the pinch region. No correction for the gas attenuation in the main DPF vessel along the 5 cm path nor in the diagnostic vessel is performed. The radiation from the pinch is reflected from a Mo/Si multi-layer mirror and is directed through a 1 μ m thick Be foil onto an un-coated IRD AXUV-100 photodiode. Details of the measurement technique are given in [8]. A typical measurement sequence consists of

recording the voltage waveforms on the pulsed power system, the DPF anode, and the photodiode as a function of the experimental parameters. Data acquisition and control of the gas system are performed via a computer interface.

The representative dependence of the in-band EUV signal (at 13.5 nm, into 2% bandwidth, into 2π sr) on the Xe flow rate is shown in Fig. 2 at a constant operating pressure of 350 mTorr and at a fixed charging voltage on the first stage capacitor of the pulsed power system. Similar behavior was observed at all operating pressures with the peak EUV signal occurring at 200 mT total pressure.

A significant increase in the EUV output from the source was observed when He was injected around the anode and Xe through the cathode at 20 Hz source operation compared with He injection into the main DPF vessel as used in [1]. Additional improvement was observed by increasing the He gas flow rate via the addition of pumping capacity. The effect of higher pumping speed is to make the EUV output less sensitive to the Xe mass flow set point and to increase the measured EUV output.

Similar measurements were performed as a function of He pressure at a constant Xe flow rate and a voltage of 1300 V on the first capacitor stage. Figure 3a shows the voltage waveform on the final stage capacitor (C2) and the in-band 13.5 nm photodiode signal for He injection around the anode. The EUV signal strongly depends on the He pressure. Examination of the C2 waveform shows that the energy recovered by this capacitor due to underdamped response depends on the gas recipe. A similar dependence was observed as a function of Xe flow variation.

The energy dissipated in the pinch region is calculated from the difference in stored energy on the C2 capacitor. At 1500 mT He pressure, approximately 70% of stored energy is dissipated in the pinch region (8.8 J), while at 200 mT, the corresponding value is 96% (11.9 J). This dependence is illustrated in Fig. 3b where the photodiode signal, initially stored energy, recovered energy and dissipated energy are plotted as a function of the He pressure. The EUV signal increases by approximately a factor of 10 over this range. A further decrease in the He partial pressure results in a sharp drop in the EUV yield not shown in these data.

Another interesting feature of the dependence on the gas pressure is the shift in the onset of EUV emission as measured by the photodiode. At the constant Xe flow conditions used, this variation of the pressure from 180 mT to 1500 mT results in a shift of 150 ns of the EUV emission. From classical snowplow and slug models of the DPF operation we expect the characteristic axial and radial transit times for the plasma shock front to scale with the square root of effective mass density. This scaling needs to be confirmed for this configuration, and the proportionality constant may be related to the effectiveness of the shock front in sweeping the mass out of the electrode region. Calculations of this effect, based on a one-dimensional snowplow model suggest that axial and radial effective masses may be significantly less than those derived from the actual gas pressure.

The dependence of the average in band EUV energy and energy efficiency on the dissipated energy at fixed gas flow conditions is shown in Figs. 4a, and 4b. These data were taken with the source conditions optimized at the peak EUV output. Lower energy input was obtained by reducing the charging voltage while leaving all other parameters fixed. The data shown here are for the optimum conditions of the present experiment as well as for the configuration presented in [1] employing a different gas recipe and anode geometry. At 10 J a 70% increase in conversion efficiency (CE) is obtained, as compared with the previous configuration. Although the energy coupled into the pinch depends on the gas recipe, we can see that the dependence of EUV energy shown in Figures 3a and 3 b is primarily due to variation in gas flow and not to the change in coupling.

Two types of measurements of the EUV radiation lying outside the 2% bandwidth around 13.5 nm were performed. The experimental setup for these measurements is shown in Figures 5a and 5b. The first type of measurement compared the total radiation from the pinch on axis with the fraction transmitted through a CaF_2 window transmitting in the 130 nm – 1300 nm band. These results show that ~0.5% of the total radiation emitted from the pinch lies in the CaF_2 band between 130 nm and 1300 nm, and are similar to those given in [8] for an earlier configuration operating at ~ 0.2% CE. In the second measurement the fraction of radiation emitted from the pinch reflected from one Mo/Si multilayer (ML) mirror and detected by the AXUV-100 photodiode was compared with the fraction of radiation transmitted through a 1 μm Be foil and reflected by the ML mirror. The signal, measured on the photodiode with no filter in place after reflection from the ML mirror gives the sum of in-band and out-of-band components. Insertion of a Be filter limits the measurement to the in-band fraction only. Therefore by subtracting the in-band fraction of radiation corrected for the ML mirror transmission from the total signal with no filter we conclude that ~ 15% of the total radiation reflected by one ML mirror is out of the 2% band around 13.5 nm.

Measurements of source size and centroid motion were performed with the source tuned for peak output. A pinhole camera employing a back-illuminated CCD array and a Be filter was used. The source images are shown in Figures 6 and 7. This arrangement was similar to that described in [7]. Measurements were taken with the camera positioned on axis, and at 68 degrees relative to the pinch axis. The average source size (averaged over 100 pulses) was determined to be 0.25 mm x 2 mm full-width-at-half-maximum. The pulse-to-pulse EUV source centroid displacement is plotted in Figure 8. The average displacement is approximately 50 μm .

Using the pinhole camera technique we can obtain an estimate of the EUV energy stability by integrating the intensity in each frame and calculating the standard deviation of this quantity. The results show 9.5% (1σ) intensity fluctuation. This measurement compares well with measurements of the energy stability performed with the standard measurements using a Be filter, ML mirror, and AXUV –100 photodiode. Additional experiments that will be performed with this diagnostic will include correlation of EUV source size with the in-band energy.

From the on-axis images we also conclude that there is no EUV production originated from an interaction of the pinch with the anode end wall. The maximum EUV intensity is observed in the center of the pinch where Xe gas is injected through an aperture in the anode. No EUV emission is observed at the periphery of the pinch where it contacts the anode end wall.

4. HIGH REPETITION RATE OPERATION

Stable operation of the source at high repetition rates is important for high exposure dose and accurate dose control. The burst mode operation of our apparatus was improved. Previously, we have reported data on the pulse-to-pulse variation of the EUV output pulse energy and on the operation of the DPF in a burst mode with 100 pulses at up to 1000 Hz repetition rate. Using a resonant charging scheme with 10 J input energy (similar to that employed by Cymer's excimer lasers), the maximum burst emission period was now increased to up to 300 pulses.

The time-integrated in-band energy of the EUV pulses was measured using the multi-layer mirror – Be foil – photodiode detection scheme described above. The in-band energy vs. pulse number data are shown in Figure 9. When the repetition rate was increased from low to high rates with no changes of the gas mixture, a severe reduction of the EUV output energy was observed with increasing burst pulse number. By making appropriate adjustments of the gas recipe it was possible to tune the output in order to obtain relatively stable EUV pulse energy for 300 pulses long bursts at a 2 kHz repetition rate. As shown in the figure, after a transient period lasting for about 10-15 pulses the output energy stays at high values for the remainder of the burst. The corresponding measured standard deviation of the energy stability in this mode is 10 %. At the present level, we have not reached any fundamental scaling limitations for high-repetition-rate operation and a further performance increase should be possible with upgraded pulsed power and thermal management schemes.

5. CHARACTERIZATION AND MITIGATION OF DEBRIS FROM PLASMA FACING COMPONENTS

We have exposed Mo and Pd coated silicon wafers to the debris produced by the DPF in an effort to evaluate the main source of the debris, and the debris deposition rate on the collector optics. The source configuration for these tests consisted of a tungsten anode, alumina insulator and brass cathode. Samples were exposed to 4×10^5 pulses at 30 Hz, at a distance of 5 cm (Mo sample) and 11 cm (Pd sample) away from the pinch. The arrangement and placement dimensions are shown in Figure 10. After exposure the samples were analyzed by Energy Dispersive X-Ray (EDX) analysis. The results, summarized in Table 1 below, show that anode (W) and insulator (O, Al) materials were found at both distances, 5 cm and 11 cm.

Element	Weight %	Atomic %
O	5	32
Al	5	19
Mo	0.5	1
Xe	2	3
W	87	55

Element	Weight %	Atomic %
O	1	2
Al	1	1.5
Si	72	90
Pd	12	4
W	12	2

Table 1. Left: (Sample 1) Mo substrate, L= 5 cm. Right: (Sample 2) Pd substrate, L=11 cm.

No sign of cathode material was observed. A small fraction of Xe was found on the Mo sample at 5 cm. This may be a signature of energetic Xe ions produced by the DPF or simply Xe incorporated into the thin film coating. The presence of He could not be detected by EDX. The presence of a weak but detectable Mo signal at 5 cm is an indication that the deposited debris is between 0.5 μm and 2.0 μm thick, which is the typical penetration depth for EDX analysis. This gives us an estimate of the debris generation rate at $1\text{--}4 \times 10^{-3}$ nm per pulse on axis at 5cm from the pinch.

A simple optical technique was tested to characterize the deposition of debris generated by the DPF. The absorption of metals in the visible region of the spectrum is generally high. The corresponding optical thickness up to which appreciable transmittance occurs is generally well below a quarter wavelength in this region so that interference fringes are not observed. According to Lambert-Beer's law:

$$T = e^{-\alpha \cdot L} \quad (1)$$

where T is the transmittance, α is the absorption coefficient and L is the film thickness. Therefore the absorbance A, defined as $\text{Log}_{10}(1/T)$, is proportional to the film thickness if α is independent of L. If L is proportional to the number of pulses, then from a measurement of the absorbance of a coating on a transparent sample due to debris produced by the DPF as a function of the number of pulses the debris deposition rate per pulse may be determined. Experimental verification of this proportionality is plotted in Figure 11.

Measurements of the absorbance allow one to compare the debris deposition rate on witness samples under different DPF operating conditions. We used this method as the primary means for obtaining the angular distribution of the debris, as well as for the debris reduction factor due to the insertion of a debris shield.

To evaluate the effectiveness of the debris shield concept a simple single-channel test setup was designed and built. The geometry and critical dimensions are shown in Figure 12. Glass samples were placed at 6cm from the pinch either facing the pinch directly or after a series of metal cylinders with 1 mm diameter channels drilled through them. Tests were performed with 1cm and 2 cm channel lengths. During the tests total pressure in the chamber was 0.7 Torr with Helium injection into the main vessel and Xe was injected through the anode. By comparing the debris film thickness using the absorbance technique, for samples which were exposed to the same number of pulses at the same operating conditions but with different debris shield lengths, we can calculate a debris reduction factor (F). If F=1 is defined as the case when the sample was placed without any protection, then F shows how effectively the debris shield protection works. Experimental results for the 1 and 2 cm thick single channel setup are plotted in Figure 14. These results show a reduction factor of 100 per cm of shield length. These results may be compared with the reduction factor measured for a more realistic multi-channel debris shield shown in Figure 13. This prototype shield was fabricated from stainless steel by electron discharge machining (EDM). The data show that under these conditions the reduction factor measured for the 1 cm long multi-channel shield was comparable to the simple 1 cm single channel setup. This gives us a measure of confidence in scaling this type of debris shield to the length required for practical source operation.

6. THERMAL ENGINEERING OF THE DPF FOR HIGH REPETITION RATE OPERATION

Water cooled electrodes, the first step in development of a thermal management solution for the DPF discharge region, have been designed and tested. These electrodes have enabled study of the DPF operation at significantly higher steady-state

repetition rates than previously achieved and generated calorimetric data that shows the dissipation of thermal energy in each electrode.

The cathode has four separate cooling delivery and exhaust loops, one for each quadrant of the annular weldment. The flow through each quadrant is arranged to be similar. It was designed to maximize the area cooled internally by the water and minimize the conduction path through the plasma heated wall and was fabricated from a high thermal conductivity copper alloy with good mechanical properties. At 400 kPa the total water flow through the cathode is 3.8 liters per minute. The water cooled electrodes are shown diagrammatically in Figure 15. The anode is cooled by flowing water through two concentric, annular channels created in the body of its welded assembly. This allows the water to get very close to the region of the part heated most aggressively by the plasma. Water can be pumped through this electrode at relatively high pressures giving high water flow rates and maintaining a more favorable temperature gradient in the region of highest heat flux. In recent testing water has been pumped through the anode at 1100 kPa giving a flow rate of 11 liters per minute.

Testing of the water cooled electrodes has been carried out up to several hundred Hertz in short bursts and at steady state repetition rates up to 200 Hz. The results so far indicate that a reasonable correlation exists between measured electrical energy input and measured heat load on the electrode cooling system when other as yet unmeasured but largely understood system heat losses are considered. The thermal energy leaving the electrodes in the water is not divided evenly between the anode and cathode. Typically the cathode removes more heat than the anode. The data suggest that the cathode removes a higher proportion of the heat as the repetition rate rises. This was expected since the anode temperature rises more rapidly than that of the cathode with increasing repetition rate and the corresponding reduction of thermal conductivity in the anode material is significant. The cathode also has a much larger cooled area, a shorter heat conduction path and far higher thermal conductivity than the anode. The fraction of heat removed by each electrode is shown in Figure 16.

Further cooling system development is underway. It is widely expected that cooling system capacity will be a limitation in ultimate performance of the DPF however it is anticipated that direct water cooling will be a useful technique for near to mid-term development of the source. A variety of high-heat-flux thermal management technologies are being evaluated including advanced systems using water.

7. SUMMARY

Significant progress has been made in all aspects of the source development. A summary of the demonstrated source parameters is given in Figure 17. In the past year we have built five new DPF sources as well as implementing upgrades to our existing 4th generation system bringing the total number of operational systems at Cymer to six. Significant improvements were made in the conversion efficiency primarily by optimization of the gas recipe and gas injection geometry. The best achieved conversion efficiency into 2π sr and 2% bandwidth was ~0.4% at ~10.5 J and low repetition rate. Stable EUV output was demonstrated for 300 pulse bursts at 2 kHz using our proven resonant charger technology. Experiments performed to date suggest that further improvement is possible by continued optimization of the gas delivery system. Energy stability continues to be ~10% (1σ) and will require improvement. Out of band radiation is < 0.5% for the improved CE source.

Characterization of debris collected on witness samples exposed to the pinch shows deposition primarily of anode material (W), and anode insulator material (Al, O). No evidence of cathode material is seen. Measurements of the debris reduction factor for single and multiple channel debris shield show a reduction factor of 100x per cm of shield length. Extrapolating this result to a reduction factor of 10^8 suggests that a 4–5 cm shield will be required.

The measurements of heat extraction from the electrodes for continuous operation at 200 Hz show that approximately 60 % of the power is dissipated in the cathode with 40% going to the anode. This suggests that at 5000 Hz repetition rate and 10 J total input energy we would need to extract approximately 20 kW from the anode electrode. At these conditions using 0.4% CE we calculate a total in band radiated power of 200 W into 2% BW and 2π sr at the source. Appropriate reduction factors must be used for all downstream components that attenuate the source radiation.

8. ACKNOWLEDGEMENTS

We would like to acknowledge the invaluable assistance of our technicians on this project without whose efforts these results would not have been possible. In particular we extend our thanks to Kevin Duenow for his assistance in all areas of the

system operation, Miguel Jaramillo for his efforts in setting up the new labs, and work in the machine shop, Terrance Houston for his work in supporting the pulsed power systems of the multiple machines used in this effort, and Vi Phung for his help in this project. We would also like to thank Mark Johnson for assisting in evaluation of the pumping configurations and for his help in keeping the labs functioning smoothly.

9. REFERENCES

1. V. Banine, and R. Moors, "Extreme ultraviolet sources for lithography applications", *Proc. of SPIE vol. 4343, Emerging Lithographic Technologies V*, ed. By E. A. Dobisz, p. 203 (2001).
2. P. Silverman, "Insertion of EUVL into high volume manufacturing", *Proc. of SPIE vol. 4343, Emerging Lithographic Technologies V*, ed. By E. A. Dobisz, p. 12 (2001)
3. U. Stamm, "High power EUV sources for lithography", presented at Sematech/ASET EUVL Source Workshop, October 29, 2001, Kunibiki Messe, Matsue City, Japan.
4. J. Pankert, "Hollow Cathode Triggered Pinch Plasma Source for EUV Lithography", presented at Sematech/ASET EUVL Source Workshop, October 29, 2001, Kunibiki Messe, Matsue City, Japan.
5. I. Fomenkov, "Development Status of a Dense Plasma Focus EUV Source for Lithography", presented at Sematech/ASET EUVL Source Workshop, October 29, 2001, Kunibiki Messe, Matsue City, Japan.
6. R. H. Moyer, et. al., "Laser Produced Plasma (LPP) Scale-up and Commercialization" in *Proc. of SPIE vol. 4343, Emerging Lithographic Technologies V*, ed. By E. A. Dobisz, p. 249 (2001)
7. W. Partlo, I. Fomenkov, R. Oliver, D. Birx, "Development of an EUV (13.5 nm) Light Source Employing a Dense Plasma Focus in Lithium Vapor", in *Proc. of SPIE vol. 3997, Emerging Lithographic Technologies IV*, ed. By E. A. Dobisz, p. 136 (2000).
8. W. N. Partlo, I. V. Fomenkov, R. M. Ness, R. I. Oliver, S. T. Melnychuk, and J. E. Rauch, "Progress Toward Use of a Dense Plasma Focus as a Light Source for Production EUV Lithography", in *Proc. of SPIE vol. 4343, Emerging Lithographic Technologies V*, ed. By E. A. Dobisz, p. 232 (2001).
9. R. Stuik, R. Constantinescu, P. Hegeman, J. Jonkers, H. Fledderus, V. Banin, and F. Bijkerk, "Portable Diagnostics for EUV Light Sources ", in *Proc. of SPIE vol. 4146, Soft X-Ray and EUV Imaging Systems*, ed. By W. M. Kaiser and R.H. Stulen, p. 121-127 (2000).

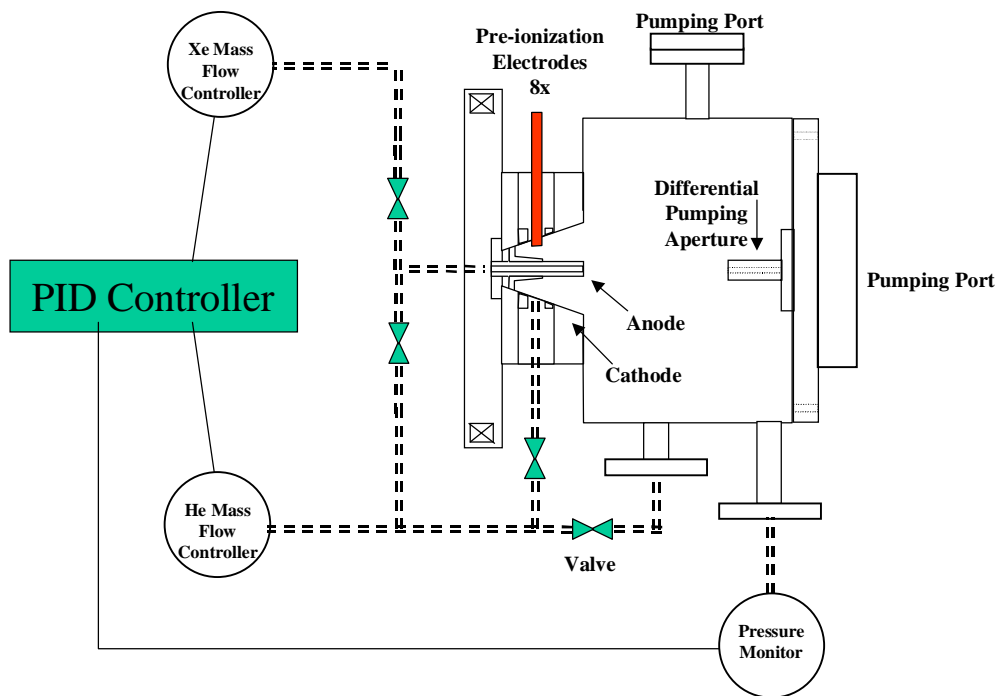


Fig. 1. Gas injection system.

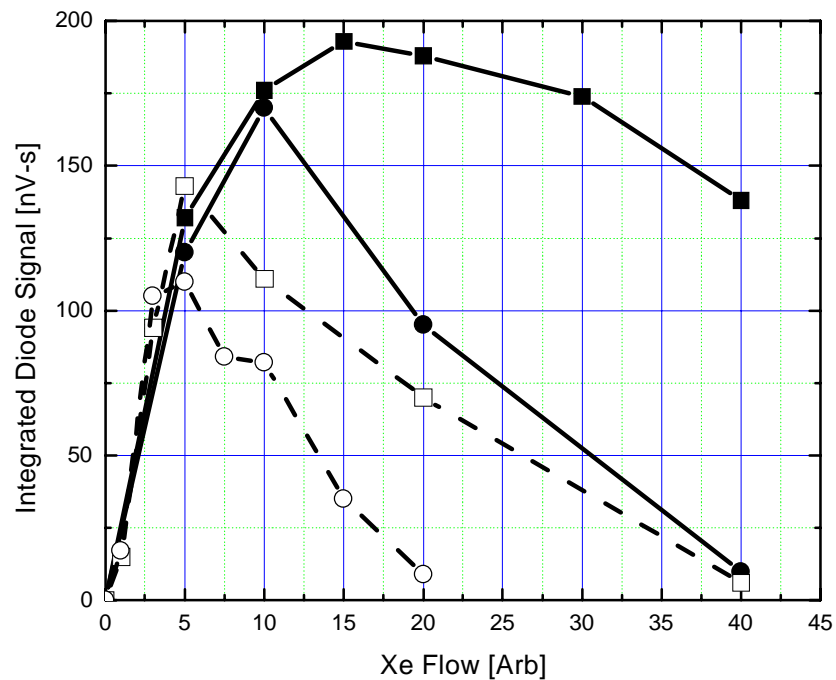


Fig. 2. In band 13.5 nm emission vs. Xe flow rate. Pressure = 350 mTorr. Symbols: Solid - He injection around anode. (■) High mass flow rate, (●) Low mass flow rate; Open - He injection into main chamber. (□) High mass flow rate, (○) Low mass flow rate.

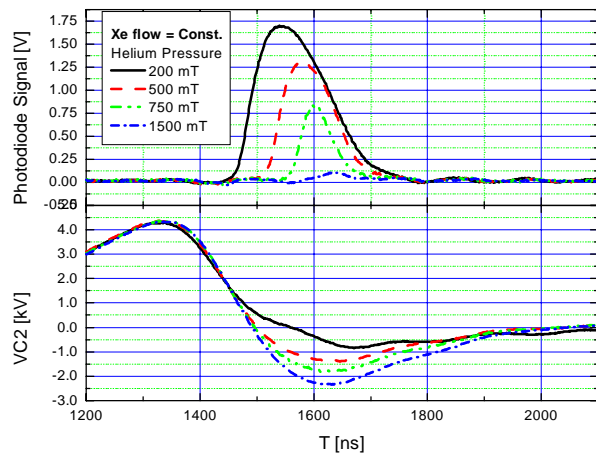


Fig. 3a. In band EUV signal at 13.5 nm and C2 voltage waveform.

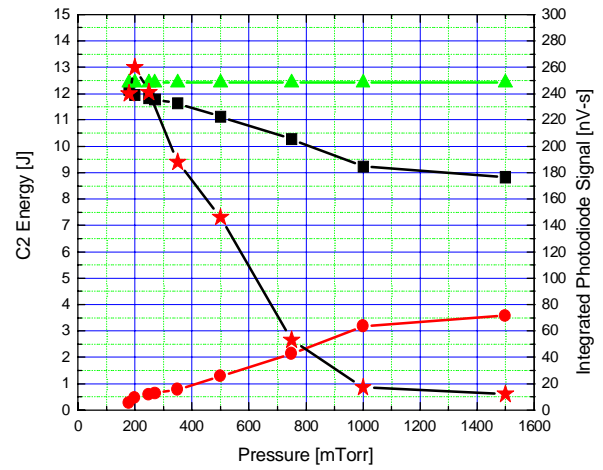


Fig. 3b. C2 total, dissipated, and recovered energy, and in band EUV signal vs. Total pressure. Symbols: (▲) Total energy; (■) Dissipated energy; (●) Recovered energy; (★) In-band EUV signal.

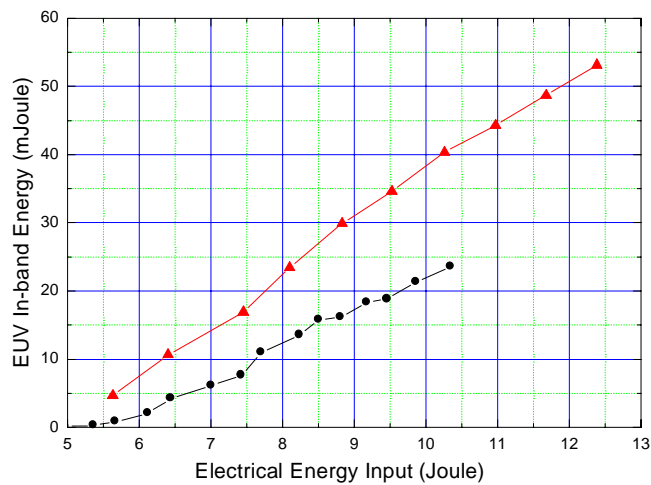


Fig. 4a. In band EUV energy vs. Input energy. Symbols: (▲) Present data with improved gas recipe and injection; (●) Data from ref. [1].

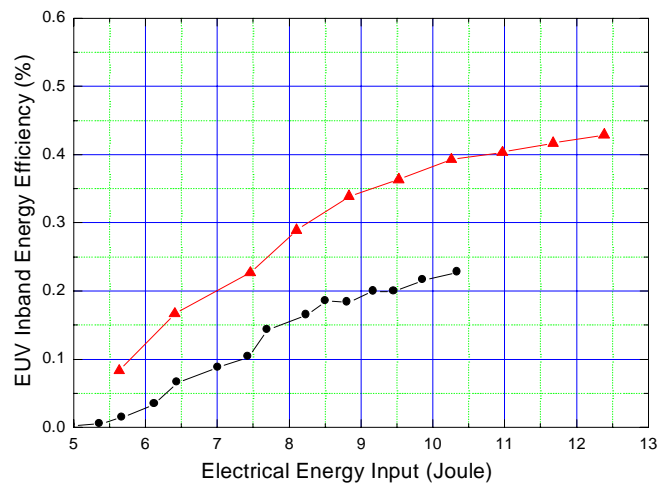


Fig. 4b. In band conversion efficiency vs. Input energy. Symbols: (▲) Present data with improved gas recipe and injection; (●) Data from ref. [1].

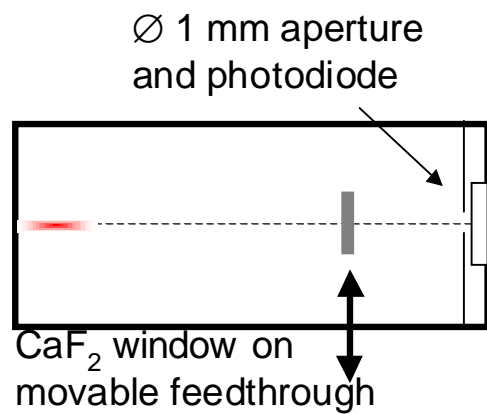


Fig. 5a. Out of band emission measurements in 130 nm – 1300 nm band.

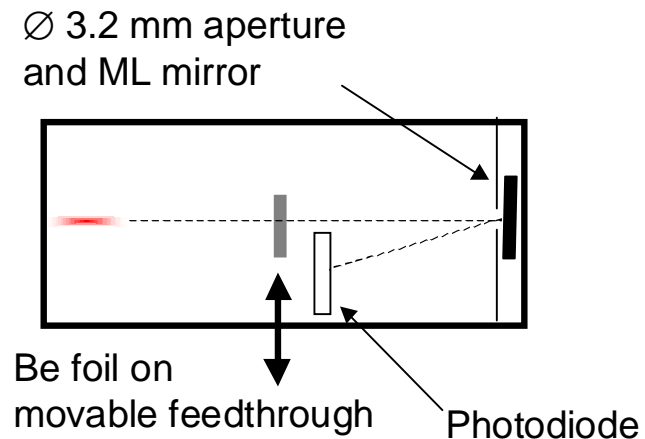


Fig. 5b. Measurements of out of band fraction of radiation reflected by on multi-layer mirror.

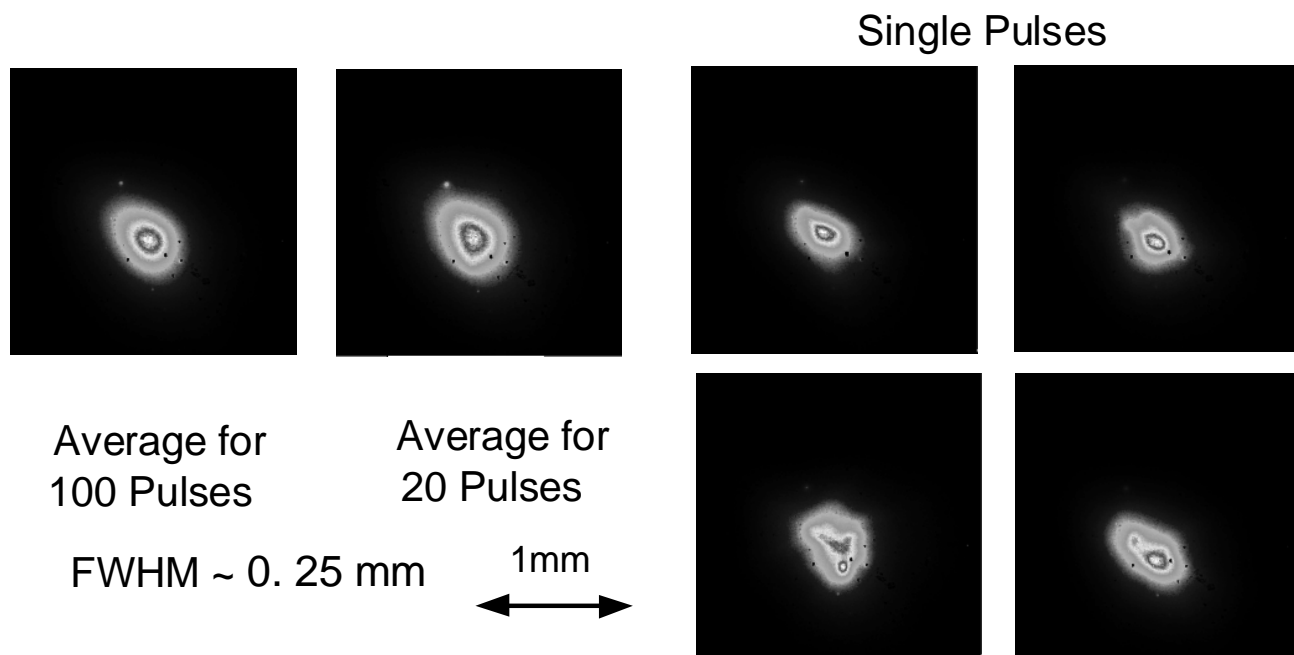


Fig. 6. EUV source image on axis. Left: 100 pulse average; Right: worst single pulses.

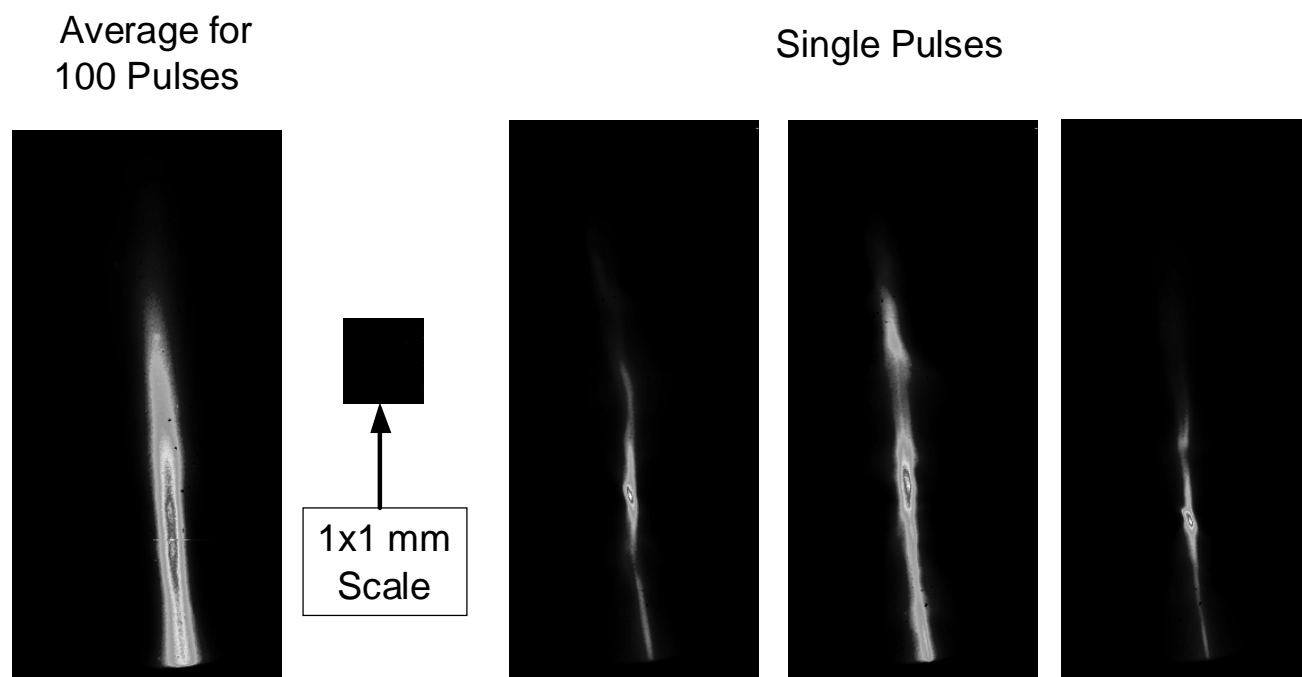


Fig. 7. EUV source image at 65 deg off axis. Left : 100 pulse average; Right: single pulses.

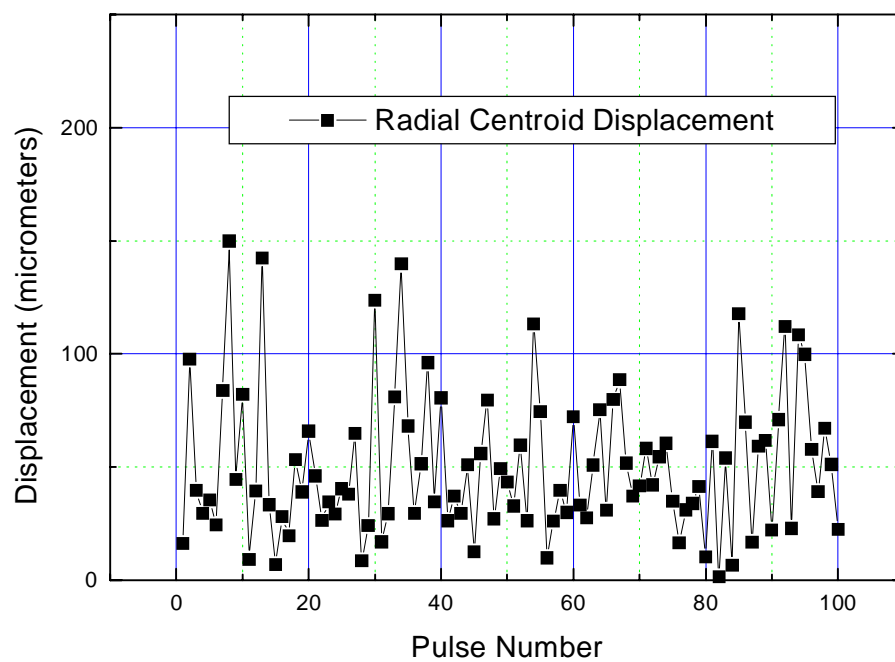


Figure 8. Radial source centroid displacement viewed on axis.

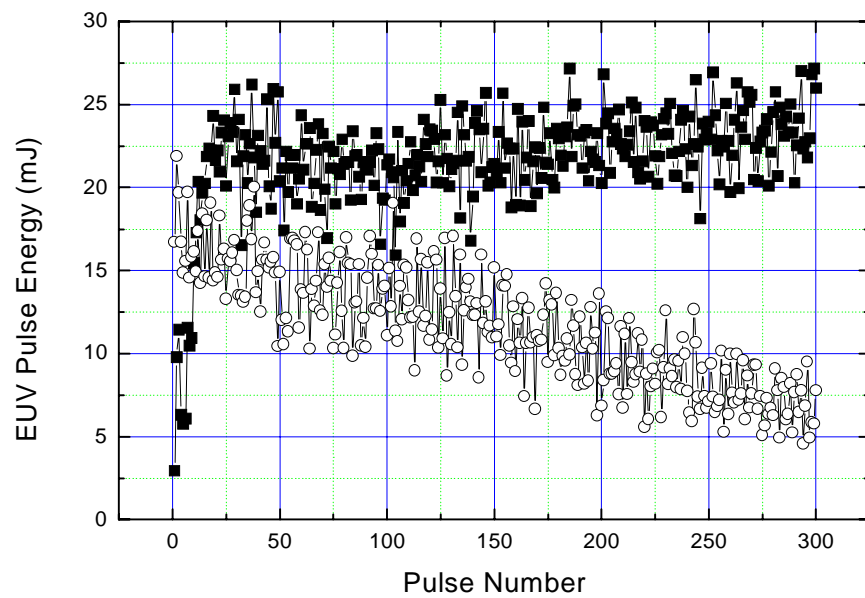


Fig.9 . High repetition rate operation. Emission into 2π , 2% bandwidth. Symbols (■) 2 kHz with optimized gas mixture; (○) 1kHz with gas mixture optimized for low repetition rate.

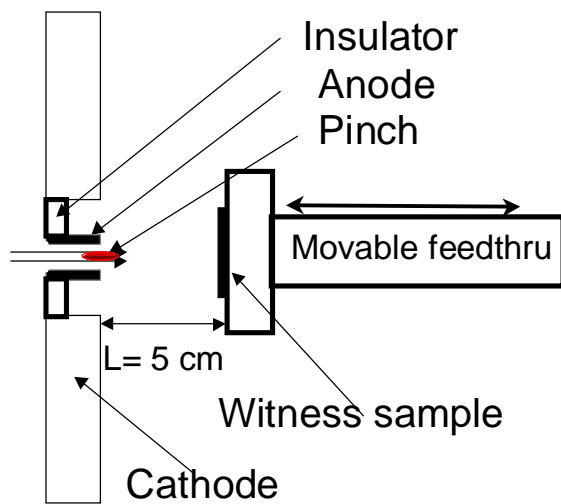


Fig. 10. Experimental arrangement for debris characterization.

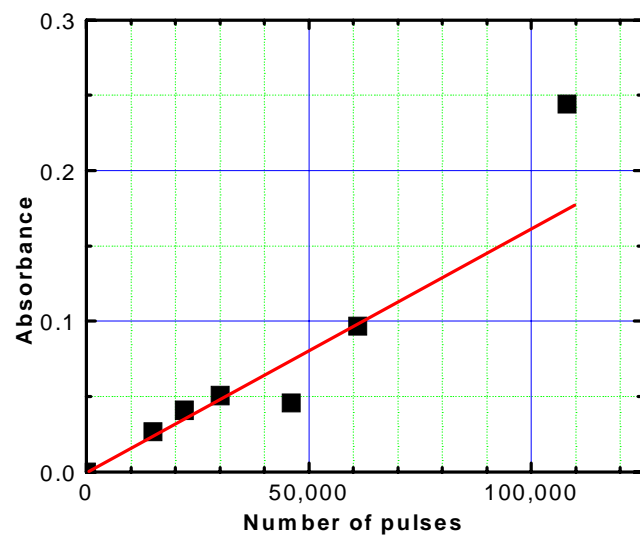
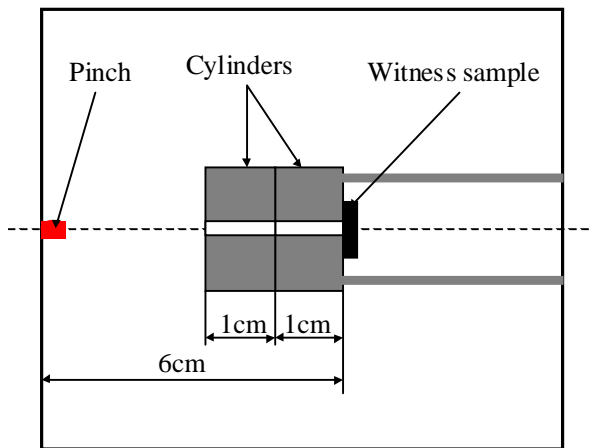
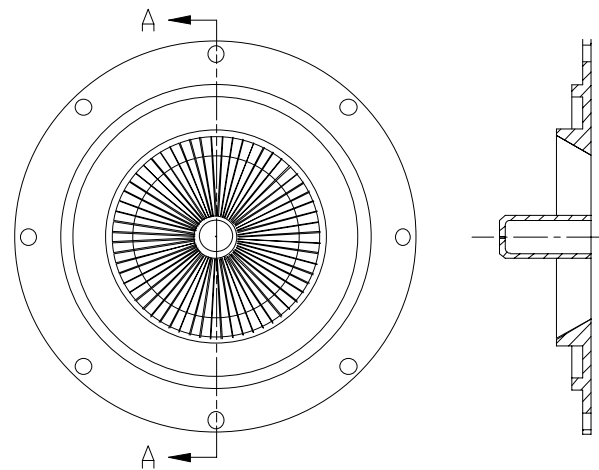


Fig. 11. Optical absorbance vs. Number of pulses.



Single channel debris shield

Fig. 12. Test fixture for measuring stopping power of single channels debris shield.



Multichannel debris shield.

Number of channels = 60. Length = 1 cm.

Fig. 13. Multichannel debris shield.

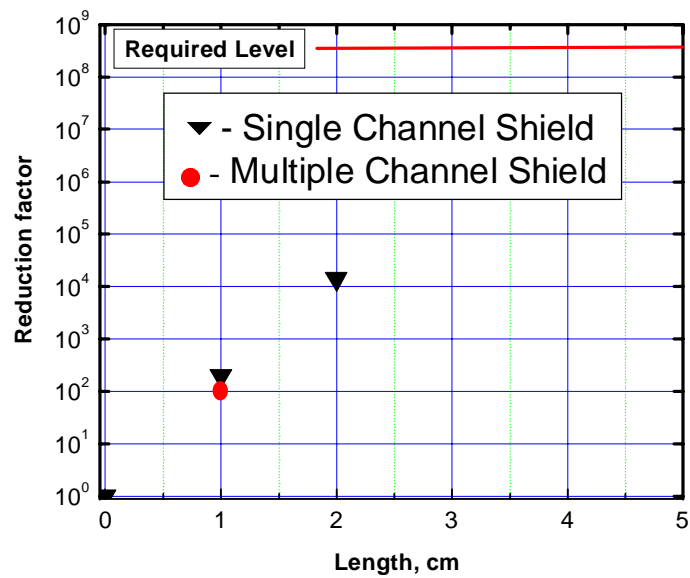


Fig. 14. Debris reduction factor vs. Channel length.

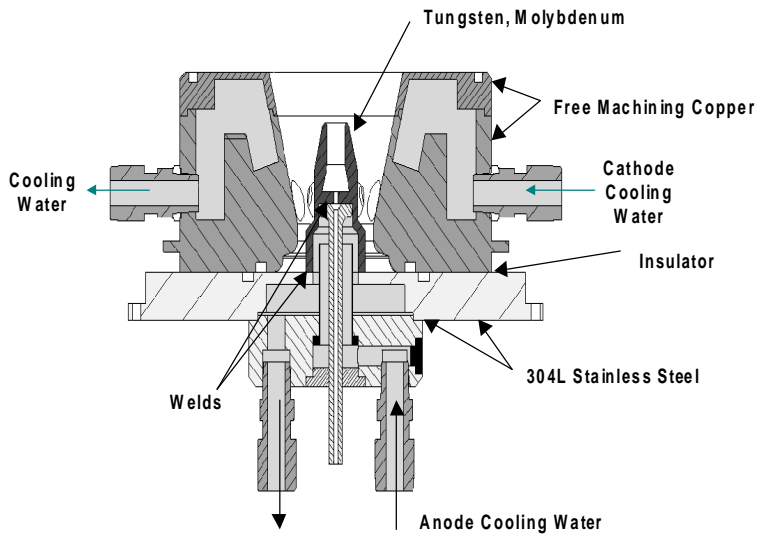


Fig. 15. Water cooled electrode design.

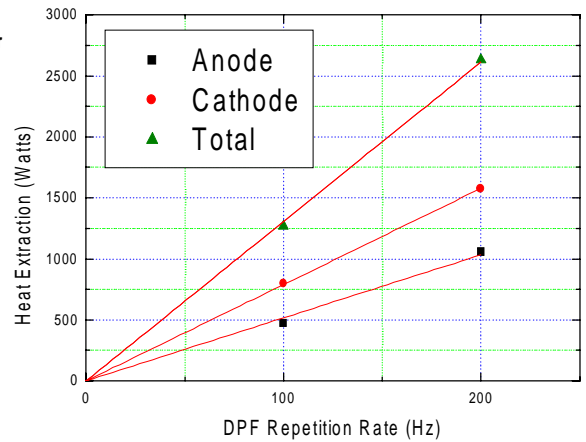


Fig. 16. Heat extraction for the DPF electrodes at 100 Hz and 200 Hz continuous repetition rate operation.

EUV efficiency with Xe,	> 0.4 %
EUV energy per pulse	45 mJ
Source size	0.25 x 2 mm
Transverse source stability	50 μ m rms
Out of band radiation	< 0.5%
Continuous repetition rate	200 Hz
Burst repetition rate	2000 Hz
Energy Stability	< 10 % rms

Fig. 17. Summary of demonstrated source operating parameters.